Supplementary Information (SI) for Soft Matter.
This journal is © The Royal Society of Chemistry 2025

Supplementary Information for: **Shape spectra of elastic shells with surface-adsorbed semiflexible polymers**

Hadiya Abdul Hameed[1], Jaroslaw Paturej[2], and Aykut Erbas[1]

[1]*UNAM – National Nanotechnology Research Center and Institute of Materials Science and Nanotechnology, Bilkent University, Ankara 06800, Turkey*

[2]*Institute of Physics, University of Silesia at Katowice, Chorzów 41-500, Poland*

1 Concentration of semiflexible chains, c

The concentration, c, of coarse-grained semiflexible chains inside the elastic shell is varied by changing the number of chains, N, within the elastic shell.

The absolute concentration, c in σ^{-3}, is calculated as

$$c = \frac{N N_{\mathrm{sf}}}{V} \tag{1}$$

where N_{sf} is the number of monomers per chain.

We also denote chain concentration in terms of bulk overlap concentration, c^*

$$c^* = \frac{N_{\mathrm{sf}}}{v} \tag{2}$$

where $v \approx l\sigma^3$ is the pervaded volume of each chain.

For $N_{\mathrm{sf}} = 8$, the overlap concentration is as follows

$$c^* = \frac{8}{\frac{4}{3}\pi(4\sigma)^3} = 0.02984155183 \approx 0.03\sigma^{-3} \tag{3}$$

$$\text{where} \quad N_{\mathrm{sf}} = 8, \qquad v = \frac{4}{3}\pi r^3, \quad r = \frac{8\sigma}{2} = 4\sigma$$

The concentrations probed for short chains (i.e., $l/R = 8/34 \approx 0.25$) are shown in Table S1. These correspond to the concentration range, $0.3c^* \leq c \leq 4.8c^*$.

Table S1: Number of semiflexible polymers, *N*, and concentrations, *c*, for N_{sf} = 8 .

N	$c(\sigma^{-3})$	c/c^*
250	0.01	0.3
750	0.03	1.0
1250	0.06	2.0
2000	0.097	3.3
3000	0.15	4.8

Since the pervaded volume of the chain, v, increases with decreasing chain length, $l = N_{\mathrm{sf}}\sigma$, the overlap concentration, c^*, decreases. For example, for $N_{\mathrm{sf}} = 32$, the overlap concentration is

$$c^* = \frac{32}{\frac{4}{3}\pi(16\sigma)^3} \approx 0.002\sigma^{-3} \tag{4}$$

$$\text{where} \quad N_{\mathrm{rod}} = 32, \qquad v = \frac{4}{3}\pi r^3, \quad r = \frac{32\sigma}{2} = 16\sigma$$

The overlap concentrations, and respective absolute concentrations in terms of c^* for various l/R discussed in the main text are shown in Table S2.

Table S2: Overlap concentrations, and normalized concentrations for various chain lengths, where $R \approx 34\sigma$.

N_{sf}	l/R	c^*	$c/c^*(c = 0.06\sigma^{-3})$	$c/c^*(c = 0.1\sigma^{-3})$
8	0.25	0.03	2.0	3.3
16	0.5	0.007	8.0	13.4
24	0.7	0.003	18.1	30.1
32	1.0	0.002	32.2	53.7
48	1.4	0.0008	72.4	120.6
64	2.0	0.0005	128.7	214.5

2 Normalized asphericity, A_{norm} The normalized asphericity, A_{norm}, is a normalized version of asphericity, A (see main text). A is normalized as follows

$$A_{\mathrm{norm}} = \frac{A}{R_{\mathrm{g}}^2} = \frac{\lambda_1 - \frac{1}{2}(\lambda_2 + \lambda_3)}{R_{\mathrm{g}}^2} \tag{5}$$

where λ_1, λ_2, and λ_3 are eigenvalues of the gyration tensor of the elastic shell, S, and R_{g} is the radius of gyration of the shell (see main text). Dividing by R_{g}^2 makes A_{norm} dimensionless, meaning that it eliminates the effect of shell size on asphericity.

The parameter A_{norm} ranges from 0 to 1: it equals 0 for perfectly symmetric (e.g., spherical) shells and approaches 1 for highly distorted shapes. In our system, A_{norm} falls within the range $0 < A_{\mathrm{norm}} \leq 0.2$, where $A_{\mathrm{norm}} \approx 0.2$ corresponds to $A \geq 100$.

3 Shape anisotropy, κ

The relative shape anisotropy, κ, is a dimensionless measure that captures both the symmetry and dimensionality of a shape[1]. It is defined as

$$\kappa = 1 - \frac{3(\lambda_1\lambda_2 + \lambda_2\lambda_3 + \lambda_3\lambda_1)}{(\lambda_1 + \lambda_2 + \lambda_3)^2} \tag{6}$$

where λ_1, λ_2, and λ_3 are eigenvalues of the gyration tensor of the elastic shell, S (see main text).

The parameter κ ranges from 0 to 1: it equals 0 for perfectly symmetric (e.g., spherical) conformations and approaches 1 for elongated, linear structures. For planar symmetric configurations, κ typically converges to 1/4.

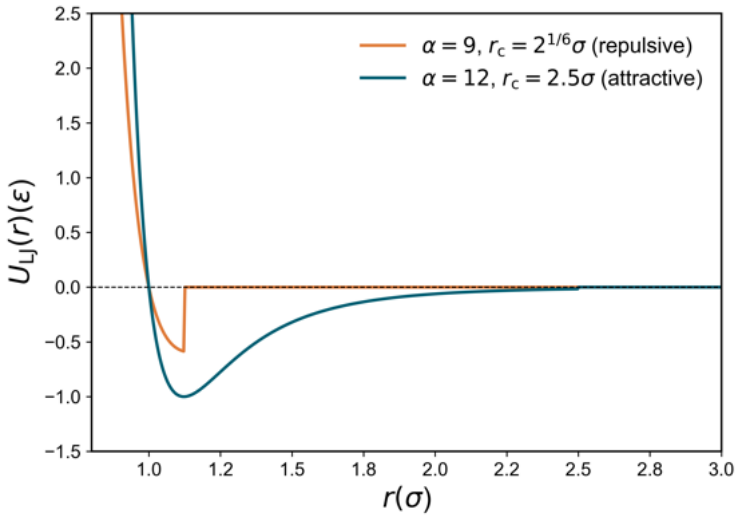

Figure S1: A shifted and truncated Lennard-Jones (LJ) potential describes all attractive and repulsive interactions (Eqn. 1 in main text). For repulsive flexible chains at the interior, we set the cutoff distance, $r_c = 2^{1/6}\sigma$ and exponent $\alpha = 9$ (orange curve). For attractive semiflexible chain-shell interactions, U_{RS}, $r_c = 2.5\sigma$ and exponent $\alpha = 12$ (blue curve)

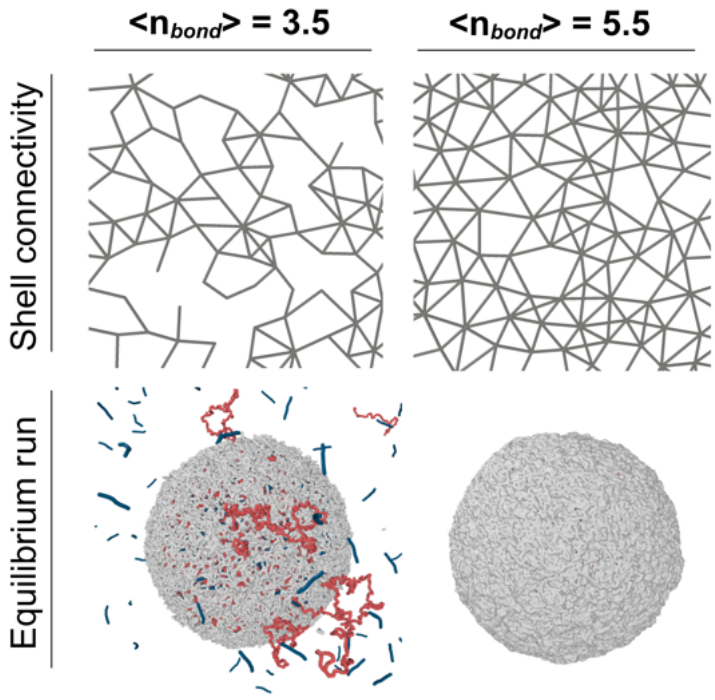

Figure S2: Decreasing shell connectivity to $\langle n_{\mathrm{bond}} \rangle = 3.5$ ($\langle n_{\mathrm{bond}} \rangle = 5.5$ in the main text) leads to the escape of shell contents during equilibrium run due to large mesh spaces.

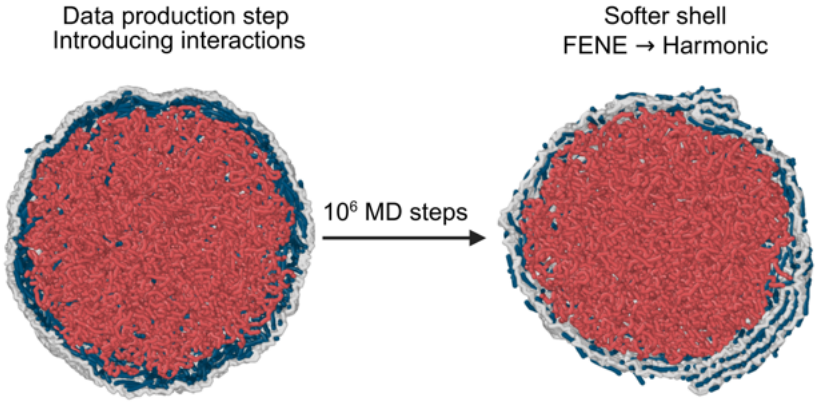

Figure S3: Replacing FENE bonds with harmonic springs to generate a softer shell configuration. These simulations are run for 10^6 MD time steps.

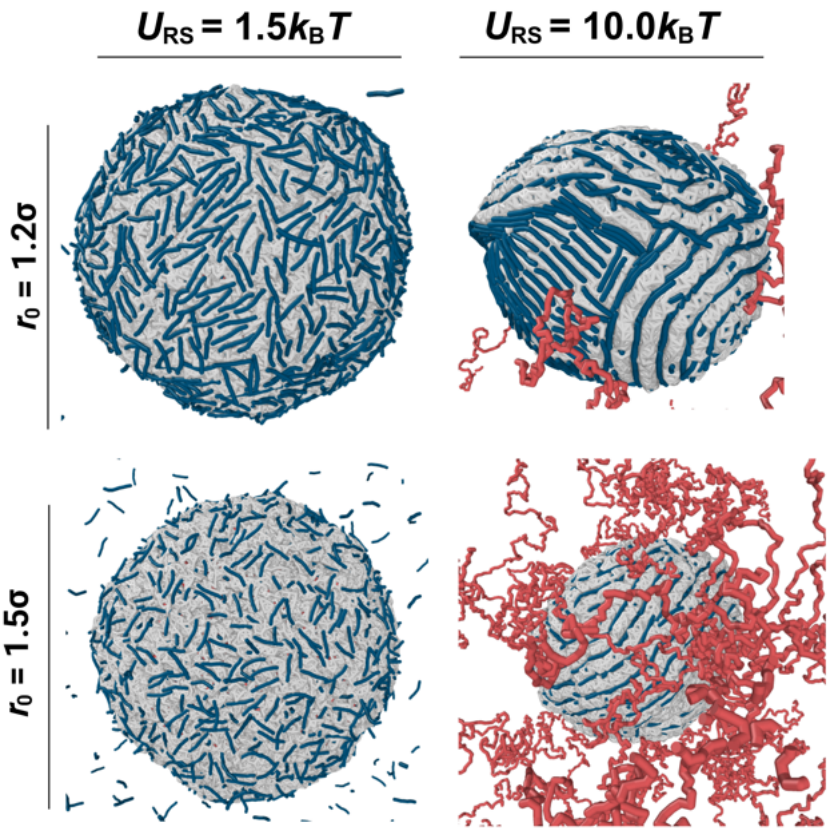

Figure S4: Reducing the cutoff distance, r_0, is required to prevent the escape of the shell contents to the exterior.

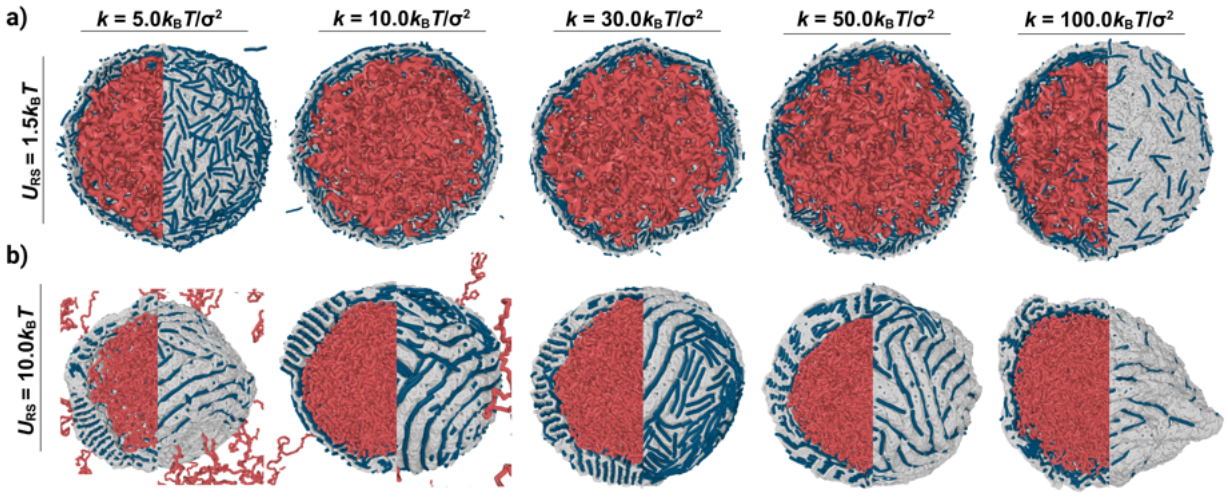

Figure S5: Effect of varying the **harmonic** shell stiffness parameter, k, over the range $5.0k_{\mathrm{B}}T/\sigma^2 \leq k \leq 100.0k_{\mathrm{B}}T/\sigma^2$, under **a)** weak and **b)** strong adsorption regimes.

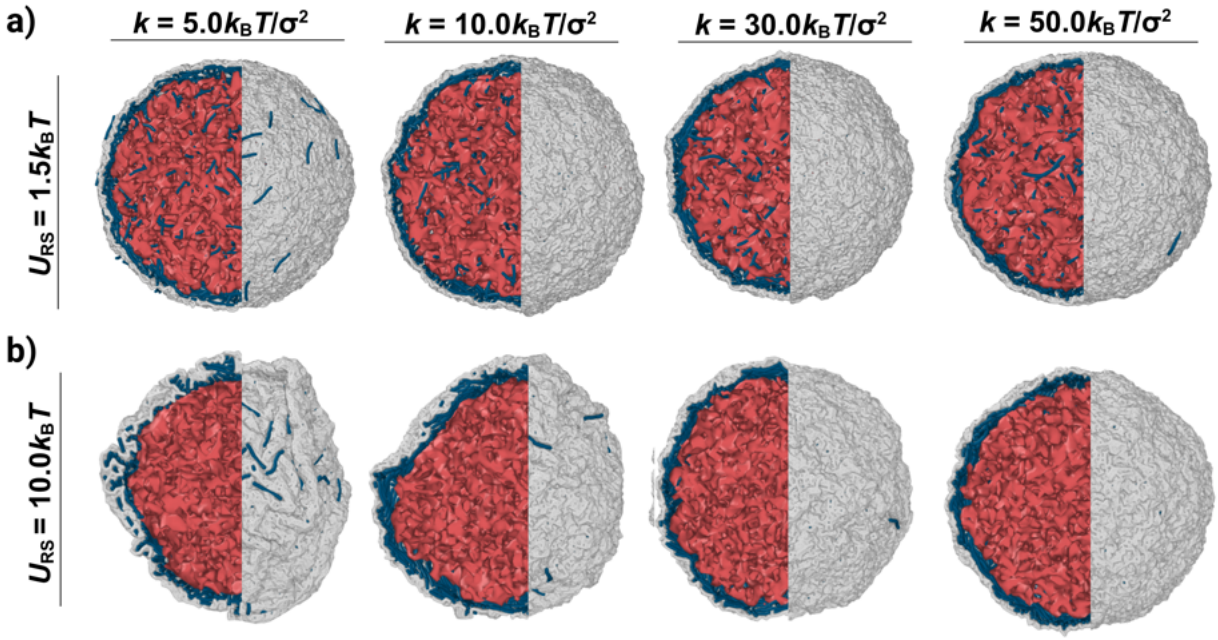

Figure S6: Effect of varying the **FENE** shell stiffness parameter, k, over the range $5.0k_{\mathrm{B}}T/\sigma^2 \leq k \leq 50.0k_{\mathrm{B}}T/\sigma^2$, under **a)** weak and **b)** strong adsorption regimes.

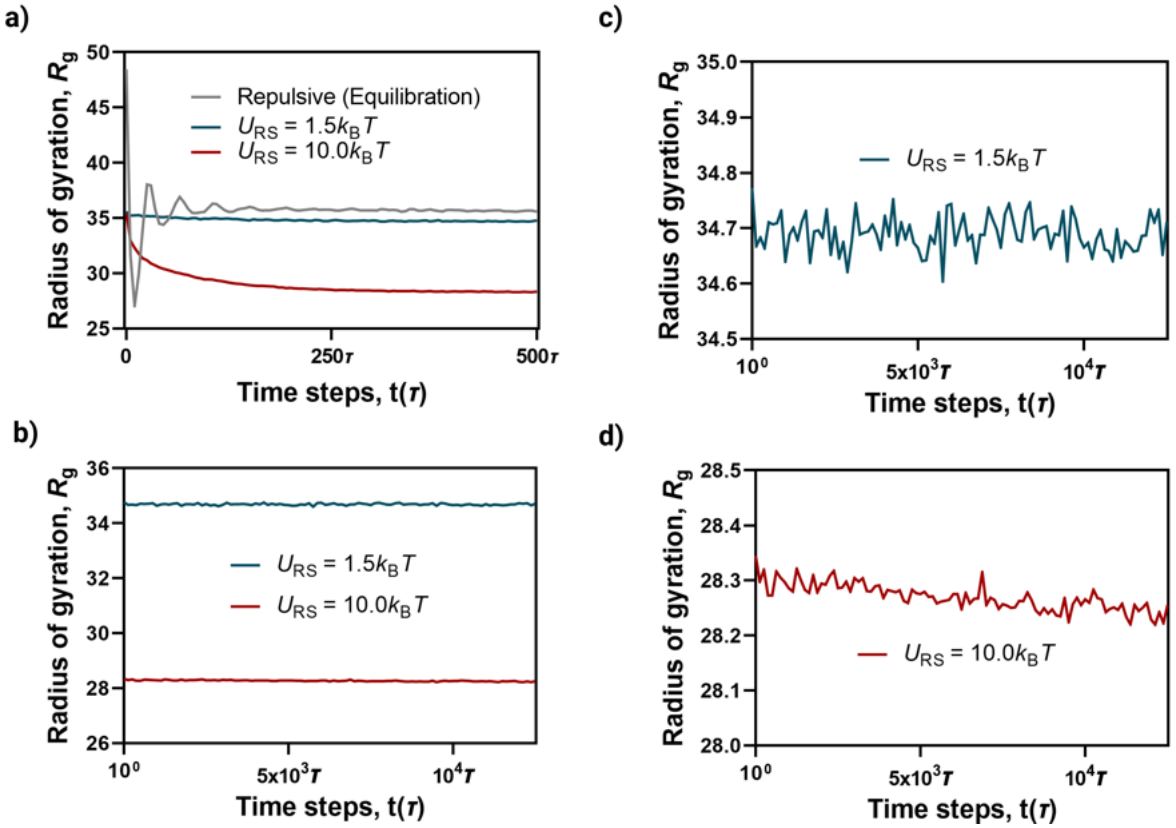

Figure S7: Radius of gyration of the shell (R_g) fluctuates within $\leq 0.25\sigma$ over simulation time for both equilibration and data production runs (see Fig. 1c), indicating quasi-equilibrium. **(a)** R_g as a function of simulation time for the equilibration step (500τ) and the first 500τ of data production runs for strong ($U_{RS} = 10.0k_BT$) and weak ($U_{RS} = 1.5k_BT$) adsorption. **(b)** R_g as a function of simulation time for the data production step ($1.25 \times 10^4\tau$). Zoomed in graphs of R_g vs. time steps for **c)** weak ($U_{RS} = 1.5k_BT$) and **d** strong ($U_{RS} = 10.0k_BT$) adsorption.

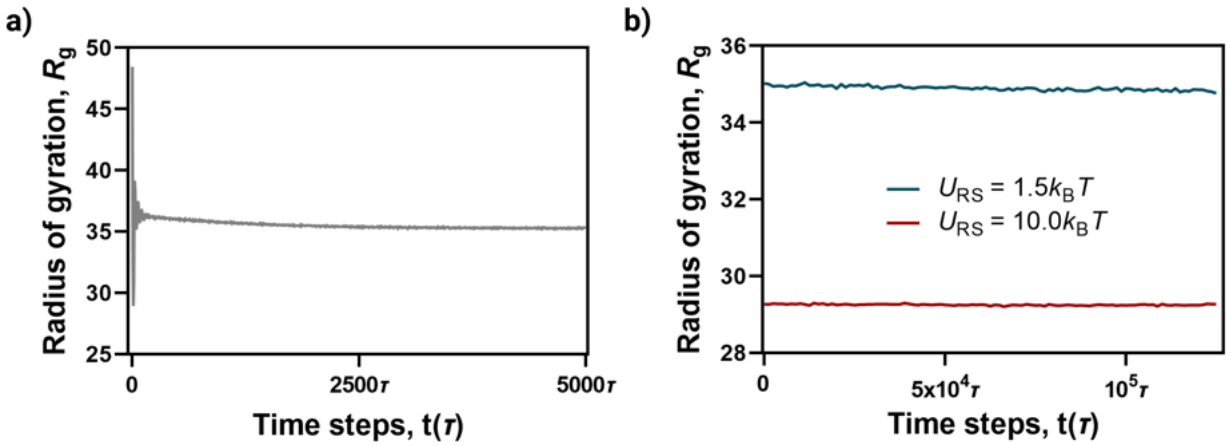

Figure S8: Radius of gyration of the shell (R_g) fluctuates within $\leq 0.25\sigma$ over longer simulation time, indicating our original simulation time is sufficient for equilibration. **a)** R_g as a function of simulation time for the equilibration step (5000τ). **(b)** R_g as a function of simulation time for the data production step ($1.25 \times 10^5\tau$).

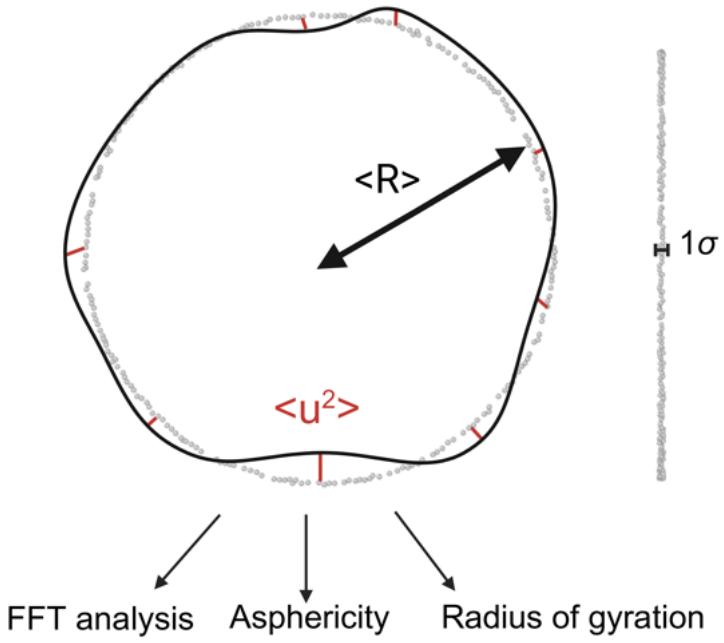

Figure S9: Analysis methods used to characterize shell shape anomalies in the main text.

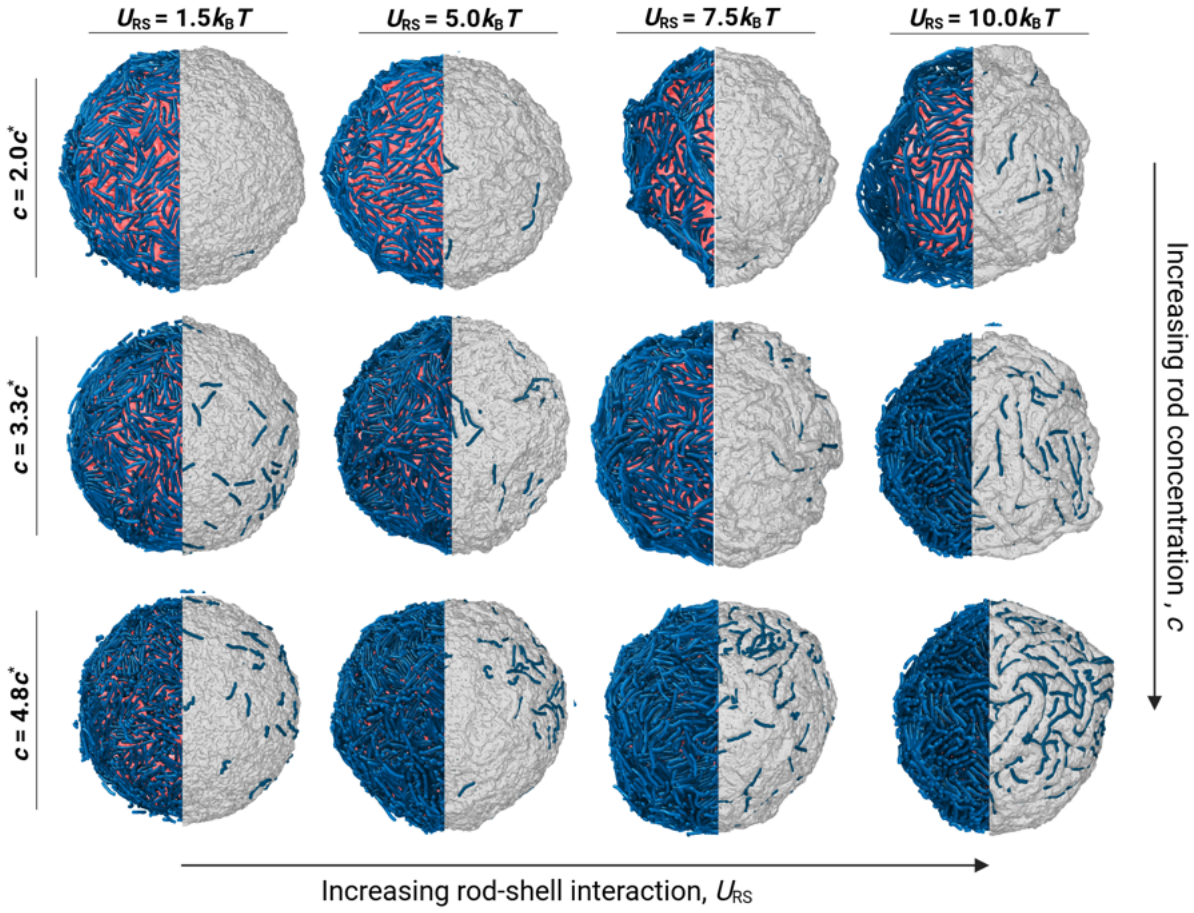

Figure S10: Exterior simulation snapshots, shell removed (right) and shell exterior(left), for various rod concentrations and U_{RS}. Shape distortions increase with increasing U_{RS} and above the overlap concentration, $c > c^*$.

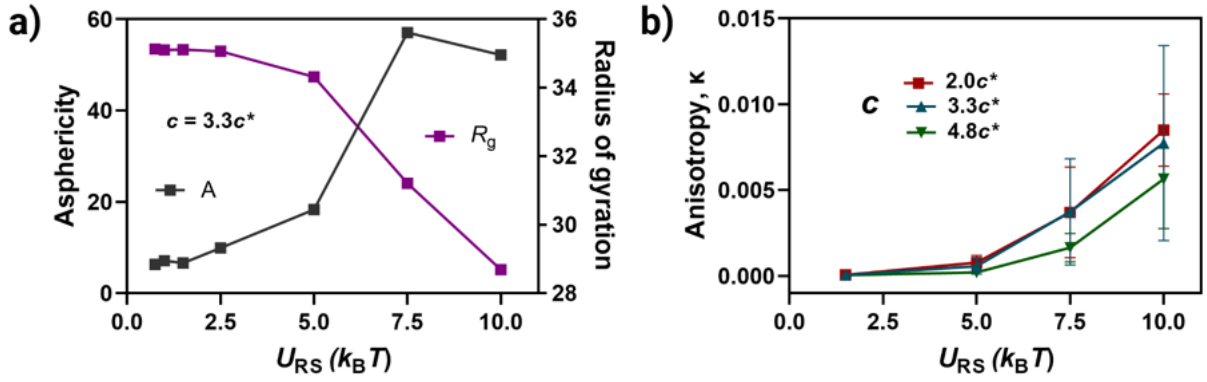

Figure S11: **a)** Radius of gyration decreases and asphericity increases with increasing rod-shell interaction strength, U_{RS}, at high rod concentration, $c \approx 0.1\sigma^{-3}$. **b)** Shape anisotropy increases as a function of U_{RS} with increasing chain concentration.

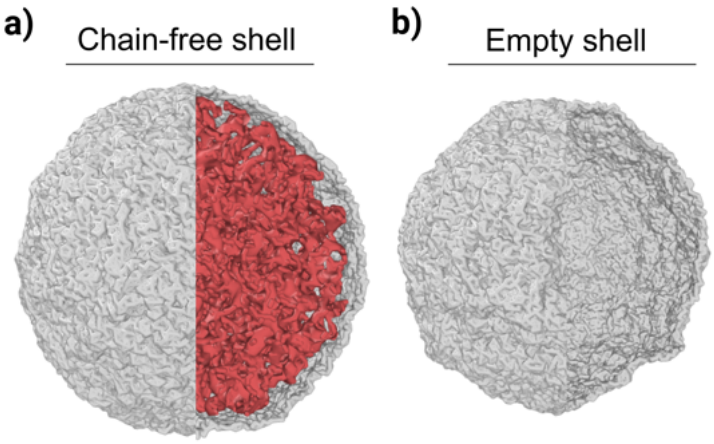

Figure S12: **a)** Two-component shell (i.e., without semiflexible chains) remains swollen (i.e., $R_g \approx 34\sigma$. **b)** Removing flexible polymer chains from the interior can also lead to crumpling and decreased size of the shell.

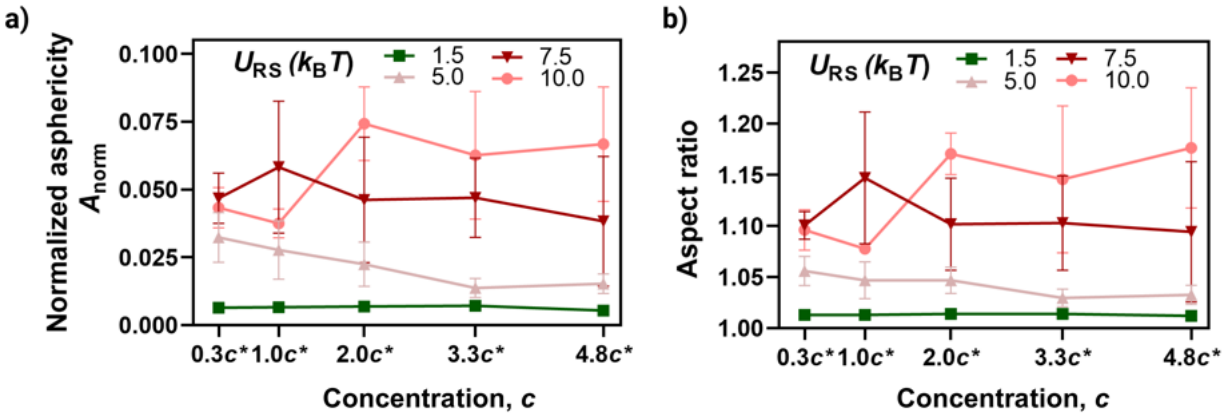

Figure S13: **a)** Normalized asphericity, A_{norm}, and **b)** aspect ratio as a function of semiflexible chain concentration, c.

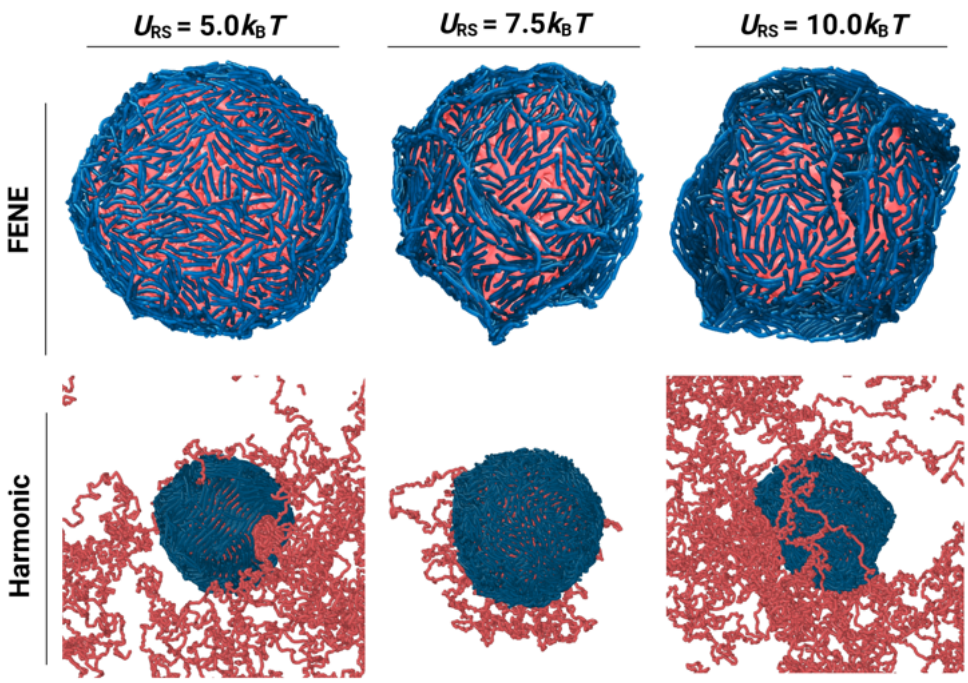

Figure S14: The elastic shell collapses inwards and polymer escapes under strong localization ($U_{\mathrm{RS}} = 5.0, 7.5$ and $10.0 k_{\mathrm{B}}T$) when shell bonds are switched from FENE to extensible harmonic ones.

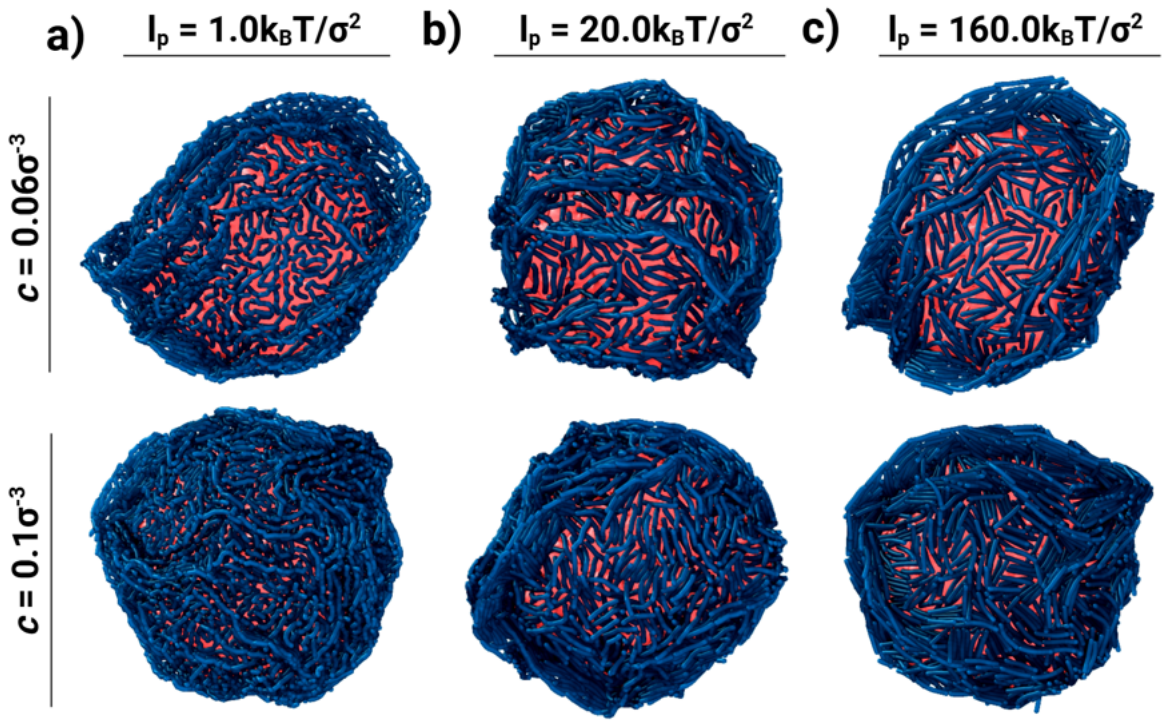

Figure S15: Distorted shapes under strong localization ($U_{\mathrm{RS}} = 10.0k_{\mathrm{B}}T$) are independent of the persistence of the chain, l_{p} at high concentrations, $c > c^*$.

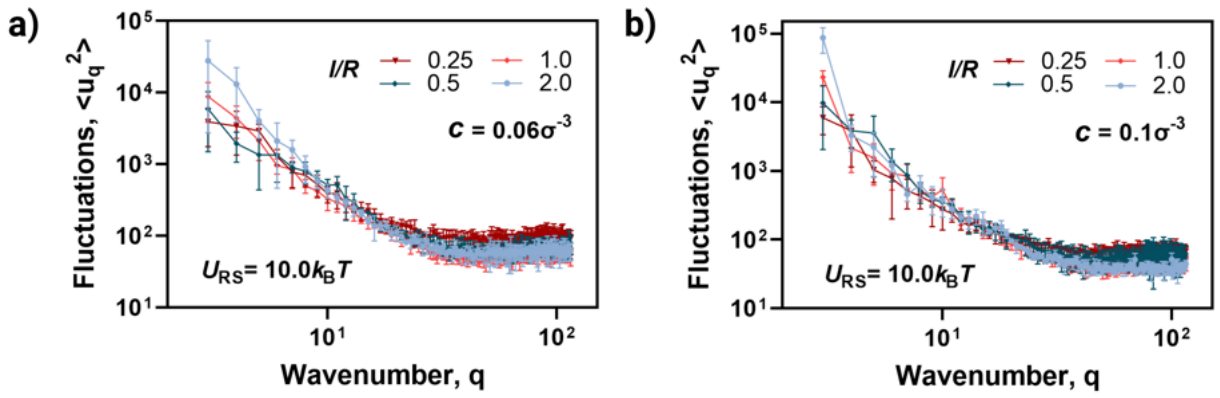

Figure S16: Fluctuation amplitudes do not vary significantly with increasing chain length, l/R, at high concentrations, $c > c^*$. Rod-shell attraction is also fixed to high, $U_{\mathrm{RS}} = 10.0k_{\mathrm{B}}T$.

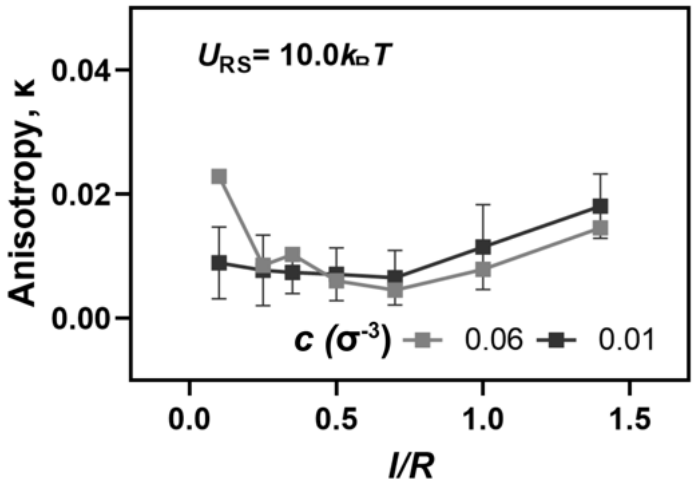

Figure S17: Anisotropy remains largely constant with increasing l/R under strong localization, $U_{\mathrm{RS}} = 10.0 k_{\mathrm{B}}T$.

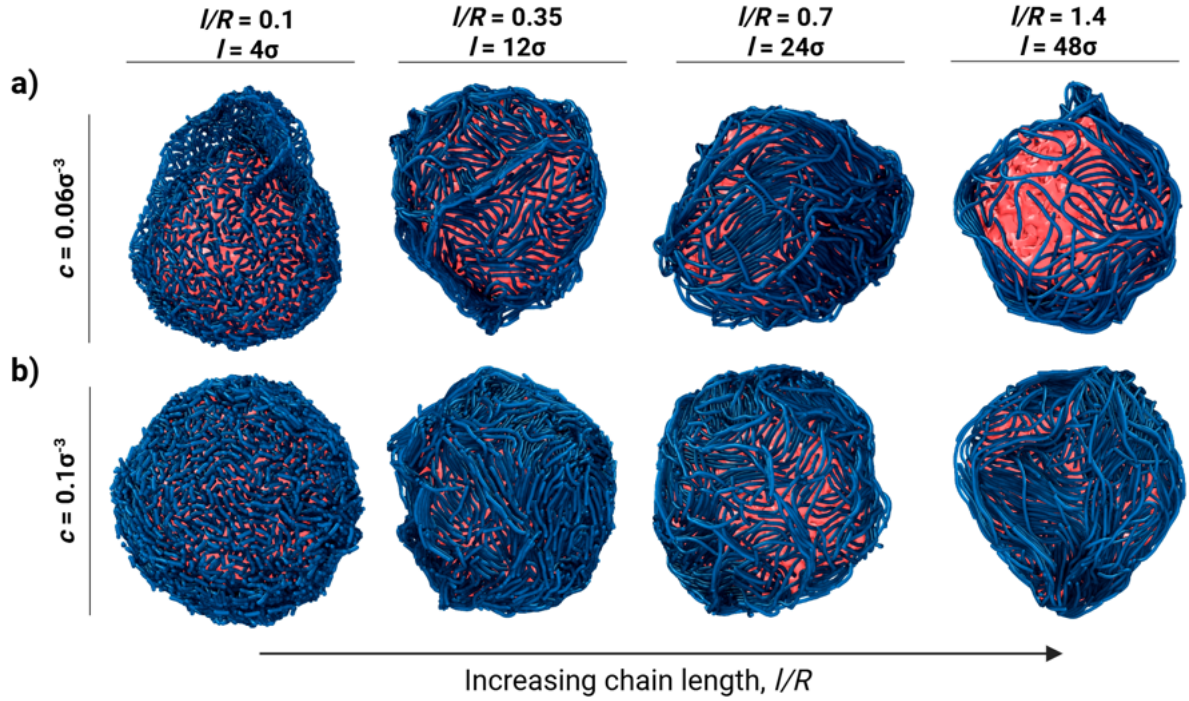

Figure S18: Simulation snapshots for distorted shell shapes at l/R = 0.1, 0.35, 0.7, and 1.4 under strong localization, $U_{\mathrm{RS}} = 10.0 k_{\mathrm{B}}T$. High concentrations ($c > c^*$) are chosen: $c \approx$ **a)** 0.06 and **b)** $0.1\sigma^{-3}$.

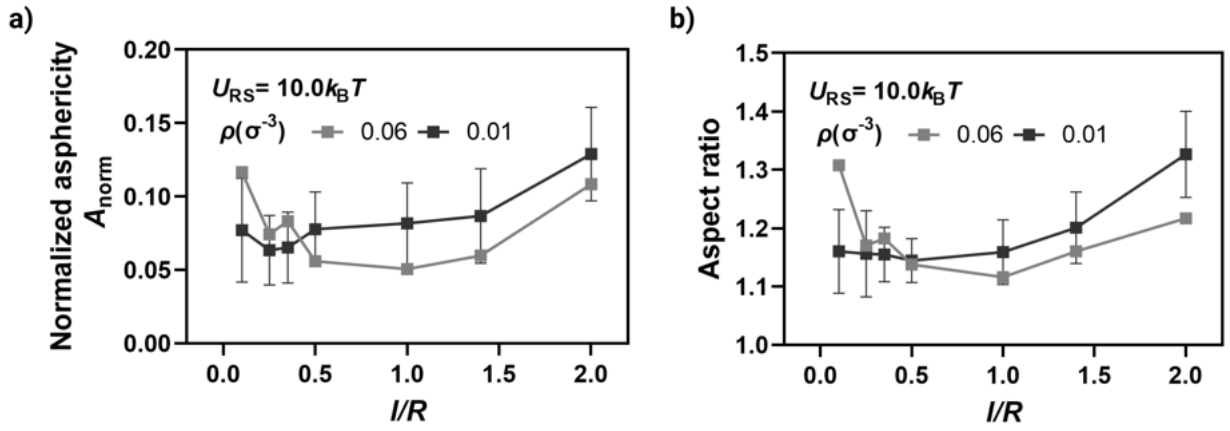

Figure S19: **a)** Normalized asphericity, A_{norm}, has larger error bars with increasing chain length, l/R. **b)** Aspect ratio exhibits slight increase with increasing l/R under strong localization, $U_{\mathrm{RS}} = 10.0k_{\mathrm{B}}T$.

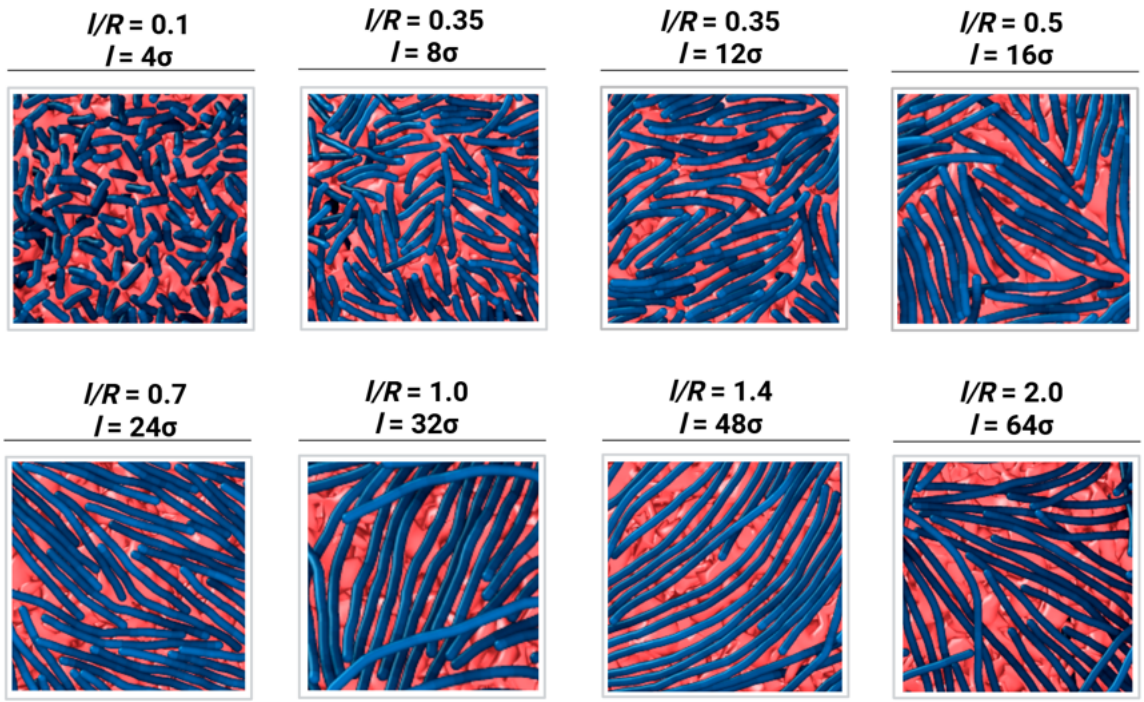

Figure S20: Organized domains emerge on the surface with increasing contour length-to-radius ratio, l/R, under weak localization, $U_{\mathrm{RS}} = 1.5k_{\mathrm{B}}T$, even at lower absolute concentrations, $c \approx 0.06\sigma^{-3}$. This also corresponds to $c > c^*$.

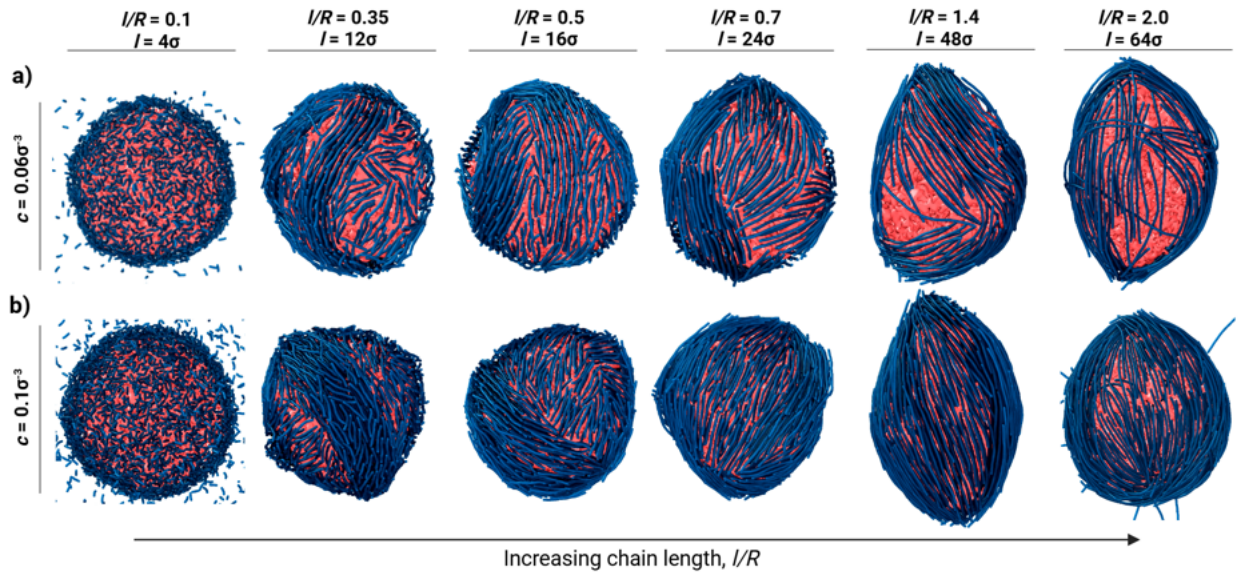

Figure S21: Shell elongates with increasing l/R under weak localization when shell bonds are switched from FENE to harmonic, irrespective of chain concentration (i.e., $c \approx$ **a)** 0.06 and **b)** $0.1\sigma^{-3}$).

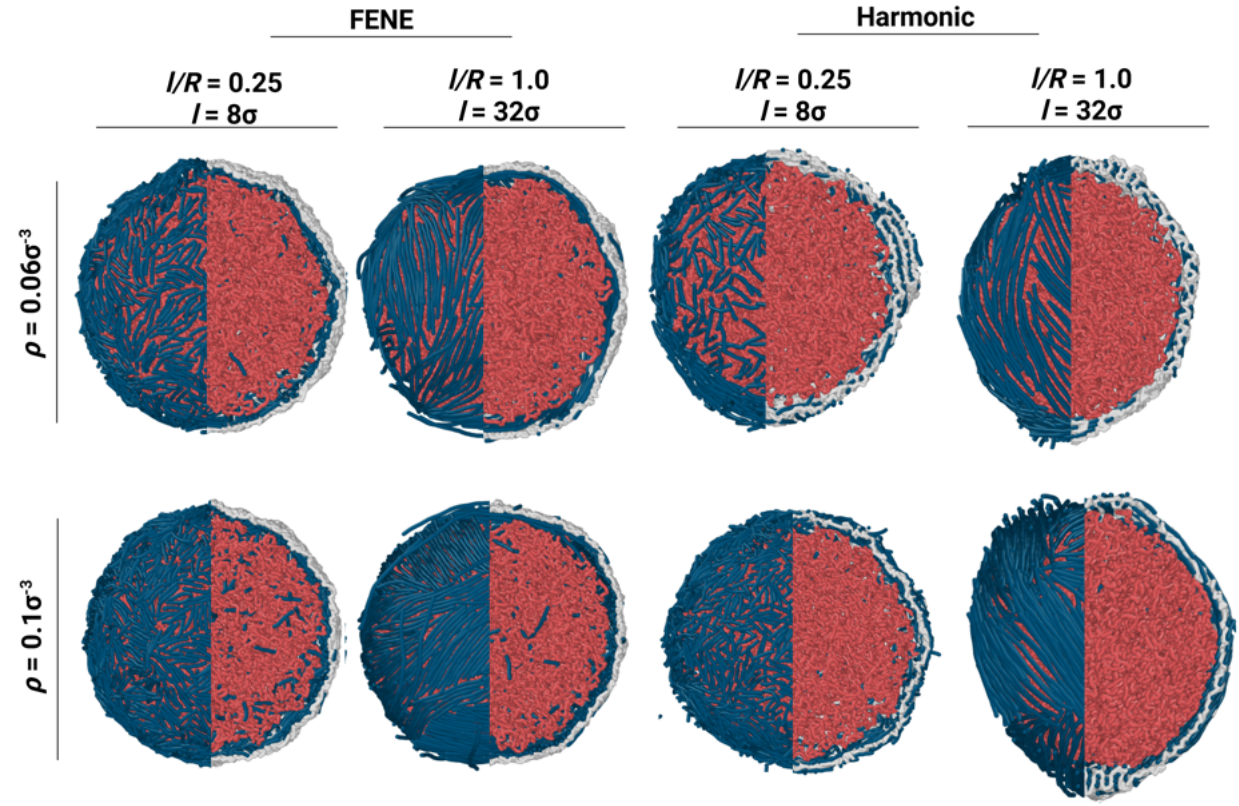

Figure S22: Exterior and interior cross-sections of the simulations discussed in Fig. 5 of the main text

References

[1] H. Arkın and W. Janke, *The Journal of Chemical Physics*, 2013, **138**,.